A Journal of the Gesellschaft Deutscher Chemiker
Angewandte Chemie
International Edition
www.angewandte.org

Accepted Article

**Title:** Ultrafast Synthesis of IrB1.15 Nanocrystals for Efficient Chlorine and Hydrogen Evolution Reactions in Saline Water

**Authors:** Tingting Liu, Zhangsen Chen, Sixiang Liu, Pan Wang, Zonghua Pu, Gaixia Zhang, and Shuhui Sun

**To be cited as:** *Angew. Chem. Int. Ed.* **2024**, e202414021

**Link to VoR:** https://doi.org/10.1002/anie.202414021

WILEY-VCH

Angewandte Chemie International Edition 10.1002/anie.202414021

RESEARCH ARTICLE WILEY-VCH

# Ultrafast Synthesis of $IrB_{1.15}$ Nanocrystals for Efficient Chlorine and Hydrogen Evolution Reactions in Saline Water

Tingting Liu,[a,c] Zhangsen Chen,[a] Sixiang Liu,[a] Pan Wang,[a] Zonghua Pu,*[a,c] Gaixia Zhang,*[b] Shuhui Sun,*[a]

[a] Dr. T. Liu, Dr. Z. Chen, S.Liu, Dr. P. Wang, Prof. Z. Pu, Prof. Prof. S. Sun
Institut National de la Recherche Scientifique (INRS), Centre Énergie Matériaux Télécommunications, Varennes, Québec, J3X 1P7, Canada
E-mail: shuhui.sun@inrs.ca
[b] Prof. G. Zhang
Department of Electrical Engineering, École de Technologie Supérieure (ÉTS), Montreal, Canada
E-mail: gaixia.zhang@etsmtl.ca
[c] Dr. T. Liu, Prof. Z. Pu
College of Chemistry & Materials Science, Fujian Normal University, Fuzhou, Fujian, 350117, China

Supporting information for this article is given via a link at the end of the document.

**Abstract:** The production of storable hydrogen fuel through water electrolysis powered by renewable energy sources such as solar, marine, geothermal, and wind energy presents a promising pathway toward achieving energy sustainability. Nevertheless, state-of-the-art electrolysis requires support from ancillary processes which often incur financial and energy costs. Developing electrolysers capable of directly operating with water that contains impurities can circumvent these processes. Herein, we demonstrate the efficient and durable electrolysis of saline water to produce chlorine gas ($Cl_2$) and hydrogen using structurally ordered $IrB_{1.15}$, synthesized through ultrafast joule heating. $IrB_{1.15}$ exhibits remarkable performance, achieving overpotentials of 75 mV for the chlorine evolution reaction (CER) and 12 mV for hydrogen evolution reactions (HER) at current densities of 10 mA $cm^{-2}$. Moreover, $IrB_{1.15}$ displays a durability of over 90 h towards both CER and HER. Density functional theory reveals that $IrB_{1.15}$ has adsorption energies significantly closer to 0 eV for Cl and H, compared to $IrO_2$ and Pt/C. Furthermore, in-situ Raman investigations reveal that Ir in $IrB_{1.15}$ serves as the active center for CER, while the introduction of B atoms to Ir lattices mitigates the formation of absorbed hydrogen species on the Ir surface, thereby enhancing the performance of $IrB_{1.15}$ in HER.

## Introduction

Chlorine gas ($Cl_2$) is a vital chemical compound, with an annual production exceeding 70 million tons. It is extensively utilized in various applications such as water treatment, organic synthesis, and polyvinyl chloride manufacturing.[1-3] The electrolysis of saline water under strongly acidic conditions (pH ~2) enables efficient chlorine evolution reaction (CER) at the anode, providing a viable approach for $Cl_2$ production.[4-6] Simultaneously, the hydrogen gas generated at the cathode through the hydrogen evolution reaction (HER) can replace carbon-based energy sources.[7-10] Achieving high activity, stability, and selectivity for both CER and HER necessitates the use of advanced electrocatalysts.[11,12] Currently, Ru/Ir oxide and Pt/C represent the state-of-the-art electrocatalyst for CER and HER, respectively.[13,14] However, noble materials incur substantial costs and exhibit limited long-term operational stability. For instance, Ru-based CER catalysts lack sufficient stability during prolonged operation due to the formation of soluble ruthenium chloride.[15] Generally, compared to Ru-based materials, Ir-based materials exhibit superior catalytic stability but lower activity.[16] Controlling the proper amount of Ir in the electrocatalysts can improve the catalytic activity while maintaining the operational stability of CER catalysts. It is crucial to concurrently mitigate the usage of Ir-based materials and enhance the CER performance to align with the sustainable development goals.

In recent years, Ir-based compounds, including oxides, phosphides ($Ir_2P$, $IrP_2$), chalcogenides ($IrS_2$, $IrSe_2$), and silicides (IrSi), have been investigated and showed high HER performance.[17-24] Beyond noble metal materials, transition metal borides (TMBs) represent another distinct family. They integrate M-M metallic bonds, M-B ionic bonds, and B-B covalent bonds, offering a diverse range of properties, including exceptional hardness, high-temperature resistance, oxidation resistance, remarkable thermochemical stability, relatively low electrical resistivity, and good mechanical properties.[25-28] To date, the systematic investigation of Ir-based ordered borides as electrocatalysts for CER and HER remains unexplored. The possible reason lies in the challenges associated with the catalyst fabrication under ambient pressure and moderate temperatures.[29]

Fortunately, the technique of Joule heating offers a rapid flash heating and colling capability to the samples, enabling ramp rates up to the order of $10^5$ K $s^{-1}$. This rapid and instantaneous temperature fluctuation completes the reaction within a few seconds. More importantly, the extremely short calcination time (in seconds) prevents the sintering and agglomeration of active components that can occur during prolonged heat treatment, ensuring rapid and effective dispersion of active atoms. This process facilitates precise regulation of the particle size, composition, and structure of the synthesized material.[30] Recently, ultrafast Joule heating has been employed to synthesize intermetallic compounds with small nanoparticle sizes, including $Pd_3Pb$, metal carbides, metal chalcogenides, nanocrystals of high-entropy alloys and 2D Materials.[31-35]

In our work, using an ultrafast Joule heating-assisted strategy, we achieved the ordered incorporation of light boron (B) atoms into Ir lattices. Thanks to the interstitial effect mediated by B, the obtained intermetallic $IrB_{1.15}$ demonstrated excellent CER and HER activity and stability in acidic media. Specifically, the $IrB_{1.15}$ exhibited remarkable performance in CER and HER, achieving overpotentials of 75 mV and 12 mV, respectively, at current densities of 10 mA cm$^{-2}$. In-situ detection techniques further unveiled that the presence of Ir in $IrB_{1.15}$ served as the active center for CER, while the incorporation of B atoms into the Ir lattices facilitated the coordination of hydrogen species on the Ir surface, thereby enhancing the HER performance of $IrB_{1.15}$. Moreover, density functional theory (DFT) calculations indicate that $IrB_{1.15}$ exhibits adsorption energies for Cl and H closer to 0 eV compared to commercial $IrO_2$. These factors contribute significantly to the enhanced catalytic activity of $IrB_{1.15}$ in both CER and HER. Additionally, the strong chemical bonding and periodic atomic arrangement in the ordered $IrB_{1.15}$ structure inhibit the dissolution and reconstruction of the active Ir, ensuring catalytic stability. Consequently, $IrB_{1.15}$ displayed excellent durability for over 90 h in both CER and HER.

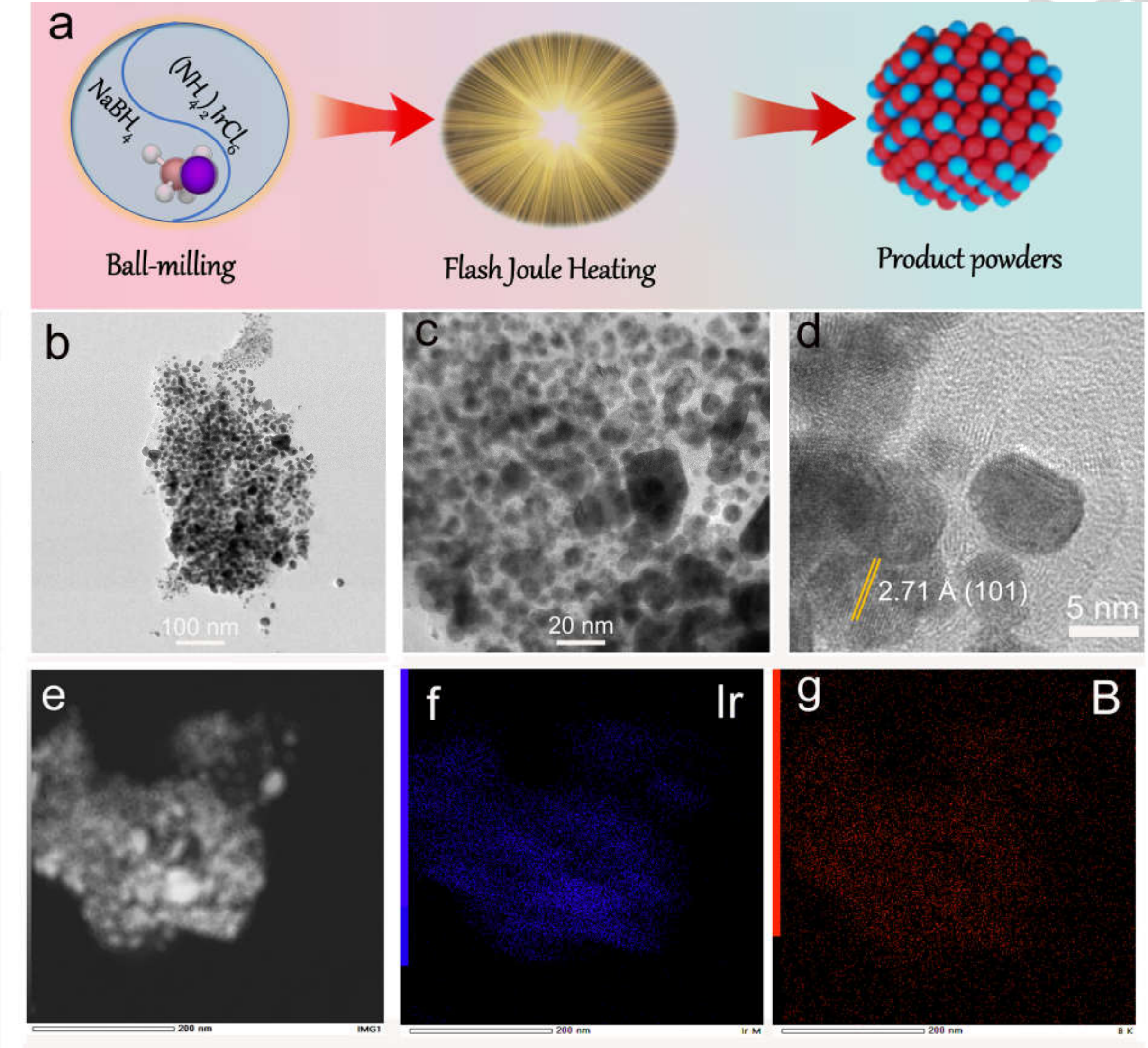

**Figure 1.** (a) Schematic illustration of the preparation of $IrB_{1.15}$. (b) Low and (c) high magnification TEM images of $IrB_{1.15}$. (d) HRTEM image of $IrB_{1.15}$. (e-g) HAADF images and EDX elemental mapping of Ir, and B, of $IrB_{1.15}$.

## Results and Discussion

The synthesis mechanism for $IrB_{1.15}$ is depicted in **Figure 1a**. First, the precursors of ammonium hexachloroirdate (IV) and sodium borohydride were thoroughly ground for approximately 10 minutes. The precursor mixture was then subjected to ultrafast Joule heating at 900 °C for 12 seconds under an argon flow. Finally, the mixture was cooled, and the byproducts ($Na^+$,

$Cl^-$, etc.) were thoroughly rinsed with deionized water. Consequently, the product of $IrB_{1.15}$ was successfully obtained.

The morphology of the $IrB_{1.15}$ sample is initially characterized using high-angle annular dark-field scanning transmission electron microscopy (HAADF-STEM). The TEM images presented in **Figures 1b-c** demonstrate the presence of numerous nanoparticles within $IrB_{1.15}$, with particle diameters ranging from 2 to 16 nm and an average diameter of approximately 4 nm (**Figure S1**). Therefore, further control should be implemented in future research to enhance the homogeneity of the resulting nanoparticles. Additionally, the HRTEM image in **Figure 1d** reveals a well-defined lattice fringe measuring 2.71 Å, which closely corresponds to the observed diffraction pattern associated with the (101) crystal plane of the tetragonal phase $IrB_{1.15}$. HAADF-STEM and EDS elemental mapping images reveal a uniform distribution of both Ir and B elements within the $IrB_{1.15}$ particle (**Figures 1e-g** and **Figure S2**). Moreover, as demonstrated in **Figures 2a** and **2b**, the atomic arrangement in specific regions exhibits remarkable conformity with the projected crystal structure along the [-110] orientation for $IrB_{1.15}$ (**Figure 2c**), as observed through HADDF and bright-field (BF) microscopy. These characterizations fully confirm the formation of intermetallic $IrB_{1.15}$ and the ordered filling of B atoms into Ir lattices.

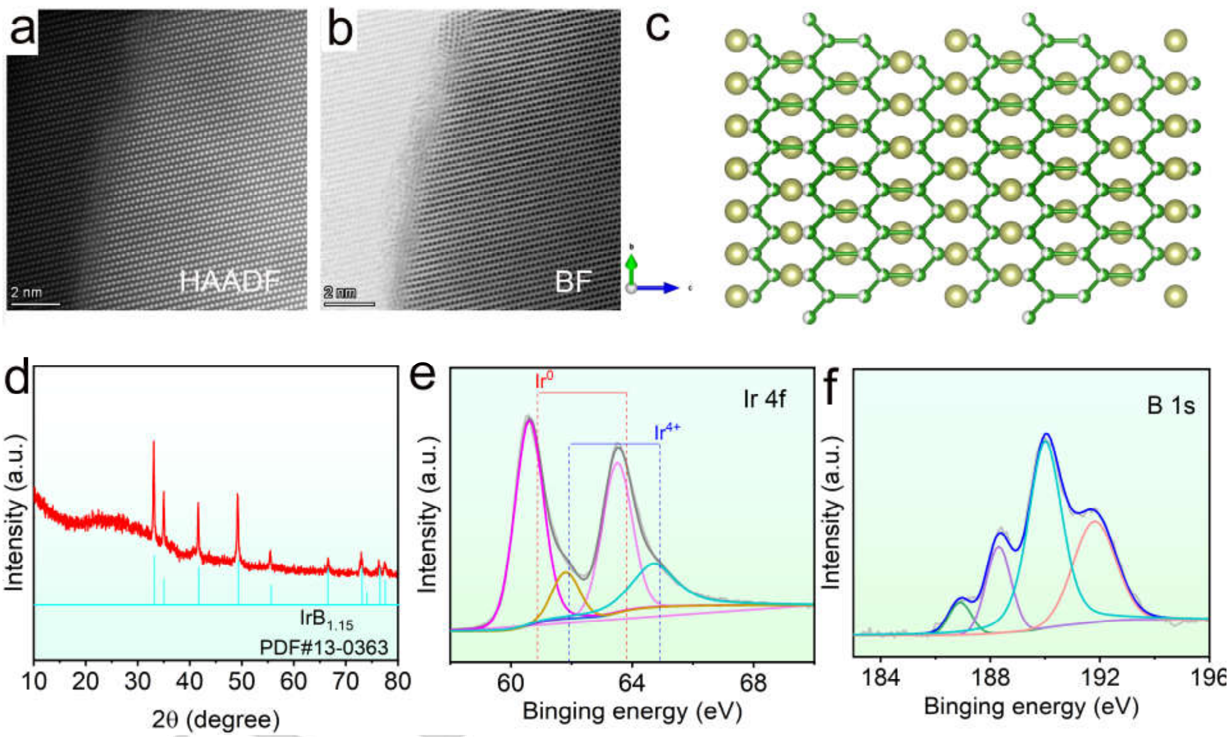

**Figure 2.** (a) HAADF-STEM and (b) BF and images of $IrB_{1.15}$. (c) Crystal structure viewed along the [-110] direction for $IrB_{1.15}$. The yellow ball reprents Ir, while bule and green ball reprents B, respectively. (d) XRD pattern of $IrB_{1.15}$. (e) Ir 4f XPS spectrum of $IrB_{1.15}$. (f) B 1s XPS spectrum of $IrB_{1.15}$.

The structure of $IrB_{1.15}$ was determined using X-ray powder diffraction (XRD). As shown in **Figure 2d**, the observed peaks at 2θ angles of 33.0°, 34.9°, 41.6°, 49.2°, 55.5°, 66.4°, 72.9°, 73.9°, 76.4° and 77.4°, can be assigned to the (101), (004), (103), (112), (105), (200), (116), (008), (211) and (204) crystal planes, respectively, indicating an tetragonal $IrB_{1.15}$ phase with the $I4_1/amd$ space group [PDF No. 13-0363, $I4_1/amd(141)$, $a_0$ = 2.81 Å, $b_0$ = 2.81 Å, $c_0$ = 10.26 Å. The X-ray photoelectron spectroscopy (XPS) survey (**Figure S3**) reveals distinct signals corresponding to the presence of B and Ir elements in $IrB_{1.15}$. In the high-resolution Ir 4f spectra (**Figure 2e**), the observed binding energies at 60.6 and 63.5 eV in the Ir 4f spectrum are consistent with those expected for $IrB_{1.15}$, specifically corresponding to the Ir $4f_{7/2}$ and Ir $4f_{5/2}$ core levels, respectively.[36] The B 1s spectrum of $IrB_{1.15}$ is presented in **Figure 2f**, wherein the two distinct subpeaks at approximately 186.9 and ~188.5 eV are ascribed to the presence of Ir−B bond within $IrB_{1.15}$, while the peaks observed at around 189.9 and 191.8 eV for the B−O bond are attributed to $BO_x$ species resulting from surface oxidation of boron.[37] It is noteworthy that following the introduction of B, the binding energy of $IrB_{1.15}$ exhibits a negative shift (~0.2 eV) in comparison to the metallic state Ir (60.8 eV).[38] The aforementioned observation implies that the introduced B atom establishes a donor-acceptor architecture with Ir based on disparities in electronegativity, thereby generating an electron-rich environment for Ir atoms.

We evaluated the CER performance of $IrB_{1.15}$ in solutions with different NaCl concentrations at pH = 2, and also conducted on commercial $IrO_2$ for comparison purposes. We found that the current densities increase with the $Cl^-$ concentrations (**Figure**

10.1002/anie.202414021

**S4**). It is worth noting that **Figure 3a** also illustrates linear sweep voltammetry (LSV) of $IrB_{1.15}$ in 0.1 M $HClO_4$ solutions (pH= 1.45, **Figure S5**). The selection of $HClO_4$ as the appropriate electrolyte is based on its suitability due to the presence of perchlorate ions ($ClO_4^-$), which are fully oxidized oxyanions of chlorine. Under anodic bias, no further oxidation of these anions occurs except for the oxygen evolution reaction (OER). As depicted in **Figure 3a**, during anodic polarization in the presence of chloride containing 4.0 M NaCl, the onset potential for $IrB_{1.15}$ is approximately 1.4 V (vs RHE, green curve), which exhibits a reduction of ~150 mV (red curve) compared to that recorded in the absence of chloride solutions (0.1 M $HClO_4$). In other words, the cathodic shift observed in the LSV under 4.0 M NaCl, as compared to that under 0.1 M $HClO_4$, suggests a significantly higher propensity for CER over OER in the chloride-containing electrolyte. Additionally, as evidenced by the LSV curves, $IrB_{1.15}$ exhibits a rapid initiation with a pronounced surge in the anodic current density. In detail, to reach a current density of 10 mA $cm^{-2}$, $IrB_{1.15}$ only requires an overpotential of 75 mV, exhibiting a Tafel slope 62 mV $dec^{-1}$, significantly lower than that observed for the commercial $IrO_2$ (89 mV and 72 mV $dec^{-1}$) (**Figures 3b** and **3c**). Furthermore, this value compares favorably with the behaviors of most Ir/Ru-based CER catalysts reported to date (**Figure 3d** and **Table S1**). The exceptional intrinsic activity of $IrB_{1.15}$ is further supported by its reduced charge transfer resistance ($R_{ct}$) and superior electrochemical surface area (ECSA) (**Figures 3e** and **3f**).[4] Specifically, Nyquist plots presented in **Figure 3e** demonstrate that $IrB_{1.15}$ has a lower $R_{ct}$ compared to commercial $IrO_2$, providing further evidence for the enhanced CER charge transfer process facilitated by B incorporation in $IrB_{1.15}$. Additionally, the cyclic voltammetry (CV) measurements conducted within a non-faradic potential range (0.75-0.95 *vs* RHE) reveal a higher ECSA of $IrB_{1.15}$, as indicated by the obtained value of double-layer capacitance ($C_{dl}$) (**Figure 3f** and **Figure S6**). This observation suggests that the incorporation of B can stimulate an increased number of accessible active Ir sites. More importantly, normalizing the polarization curves by ECSA and the mass of Ir further indicates $IrB_{1.15}$ also possesses high intrinsic catalytic activity toward CER (**Figure S7**). It is noteworthy that the $Cl_2$ selectivity serves as another crucial criterion for CER electrocatalysts in the chlor-alkali industry, which was assessed here using the rotating ring-disk electrode (RRDE) technique. As depicted in **Figure S8**, $IrB_{1.15}$ exhibits an impressive $Cl_2$ selectivity of 98.3%. The high $Cl_2$ selectivity of $IrB_{1.15}$ can be attributed to its superior catalytic efficiency for CER, which surpasses that of the competing OER.

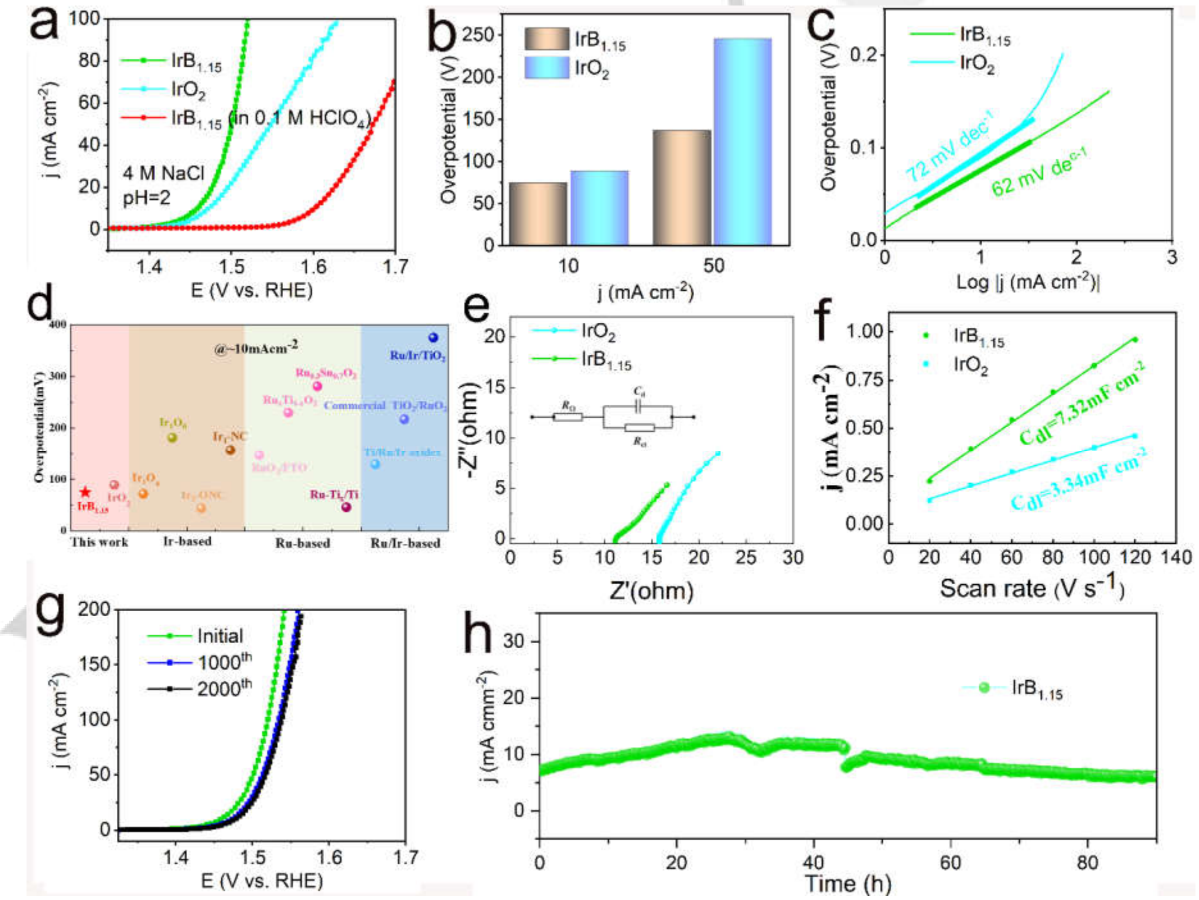

**Figure 3.** (a) OER polarization curves of $IrB_{1.15}$ and $IrO_2$ in 4.0 M NaCl at pH =2. (b) Corresponding overpotentials for $IrB_{1.15}$ and $IrO_2$ at 10 and 50 mA $cm^{-2}$, respectively. (c) Tafel slopes for $IrB_{1.15}$ and $IrO_2$ in 4.0 M NaCl at pH =2. (d) Comparison of overpotential with different representative catalysts. (e) Nyquist plots for $IrB_{1.15}$ and $IrO_2$ at an overpotential of 50 mV in the frequency range of $10^5$-0.01 Hz. (f) $C_{dl}$ of $IrB_{1.15}$ and $IrO_2$. (g) Polarization curves for $IrB_{1.15}$ before and after 1000, 2000 CVs. (h) Chronoamperograms measurements of $IrB_{1.15}$ at potential of 1.46 V vs. RHE (without iR correction).

More importantly, the polarization curves before and after 1000, and 2000 CVs are illustrated in **Figure 3g**. After 2000 CV cycles, the polarization curve for $IrB_{1.15}$ presents a slight degradation. For comparison, $IrO_2$ was also evaluated under identical conditions (**Figure S9a**). Notably, the LSV of $IrO_2$ exhibits a negative shift of approximately 16 mV after only 1000 CV cycles to achieve a current density of 10 mA $cm^{-2}$, indicating a substantial decline in its performance. Furthermore, the chronoamperometry curve of $IrB_{1.15}$ (**Figure 3h**) and commercial $IrO_2$ (**Figure S9b**) demonstrates that $IrB_{1.15}$ possesses accelerated degradation stability with minimal activity decay during extended operation over a period of 90 h. It is interesting to note that the current density of the $IrB_{1.15}$ exhibits an initial increase followed by a subsequent decrease, which may be attributed to the electrochemically activation process of the $IrB_{1.15}$. As shown in **Figure S10**, the high-resolution Ir 4f and B 1s XPS spectra of the fresh sample and $IrB_{1.15}$ after activation are similar, suggesting that the materials composition is preserved. However, a slight decrease in signal intensity at around 188.5 eV for the activated $IrB_{1.15}$ catalyst compared to the fresh sample indicates possible oxidation of some B atoms during the CER activation process. Additionally, the slight decrease in current density can be attributed to the desorption of some particles from electrode surface. Due to vigorous gas evolution, the stability of most powdered materials under CER conditions is typically low as effective strategies to securely immobilizing these materials on electrode surfaces remain limited.[39]. This good stability of $IrB_{1.15}$ after CER testing is further confirmed by the TEM image, which reveals the preservation of its original morphology structure (**Figure S11**). Moreover, the XRD patterns obtained after the stability test reveal no evidence of any additional impurity phase, thereby confirming the exclusive presence of $IrB_{1.15}$ (**Figure S12**). Thus, it is evident that $IrB_{1.15}$ achieves a good balance between activity and stability for CER.

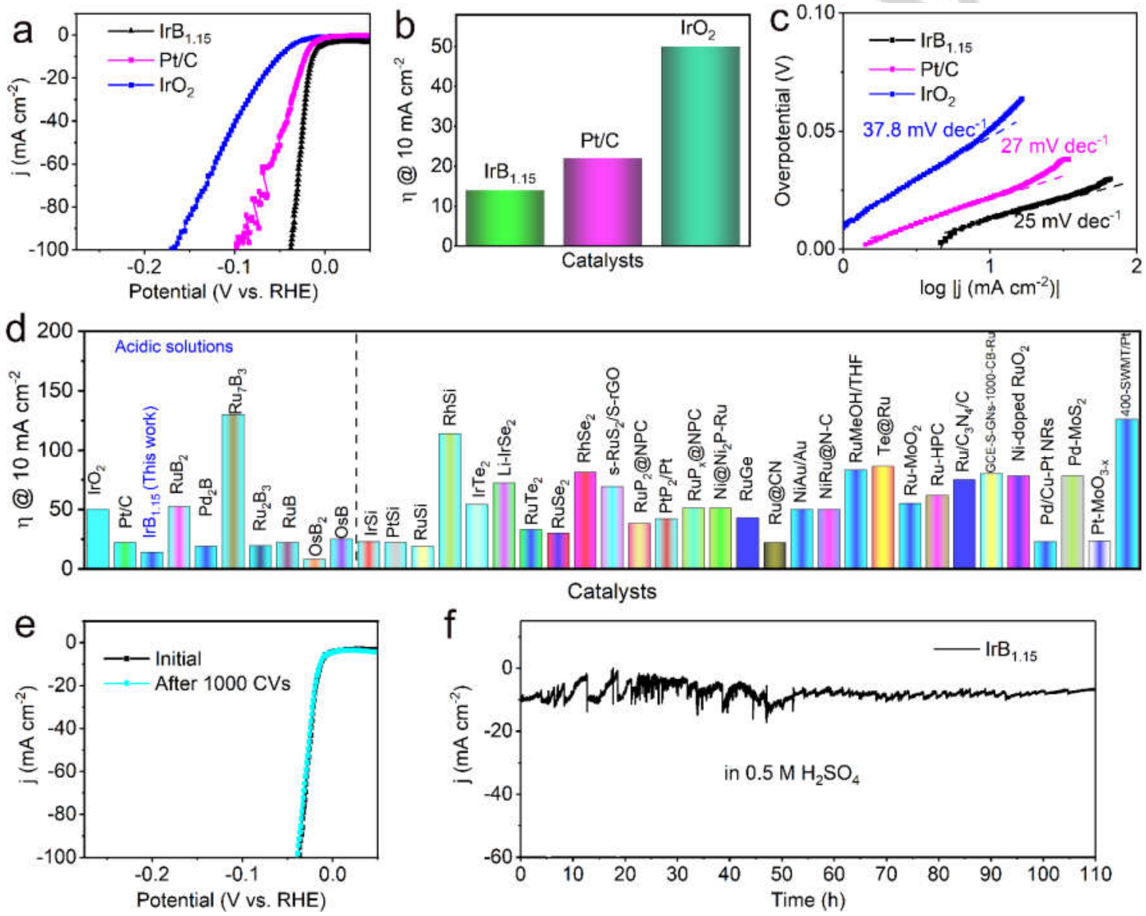

**Figure 4.** (a) HER polarization curves of $IrB_{1.15}$, $IrO_2$, and Pt/C in 0.5 M $H_2SO_4$ solutions. (b) Corresponding overpotentials at 10 mA $cm^{-2}$ for $IrB_{1.15}$, $IrO_2$, and Pt/C in 0.5 M $H_2SO_4$ solutions. (c) Tafel slopes for $IrB_{1.15}$, $IrO_2$ and Pt/C. (d) Comparison of overpotential with different representative catalysts. (e) Polarization curves before and after 1000 CVs. (f) Chronoamperograms measurements of $IrB_{1.15}$ in 0.5 M $H_2SO_4$.

In general, the electrolysis of saline water under highly acidic conditions leads to the generation of $Cl_2$ at the anode, while simultaneously producing $H_2$ at the cathode. The evolved hydrogen gas was first confirmed using gas chromatography (GC-9790 Plus, Fuli) equipped with a thermal conductivity detector (TCD) (**Figure S13**). Therefore, we further evaluated the HER performance of $IrB_{1.15}$ in 0.5 M $H_2SO_4$ solution. For comparison, commercially available 20 wt% Pt/C and $IrO_2$ were employed as reference materials. Before conducting the HER tests, the $IrB_{1.15}$ catalyst was subjected to activation through multiple cycles of LSVs within the voltage window applied for HER. As displayed in **Figure 4a**, the $IrB_{1.15}$, $IrO_2$, and Pt/C materials demonstrate excellent HER performance. The overpotentials vs. RHE at a geometric current density of 10 mA $cm^{-2}$ for Pt/C, $IrB_{1.15}$, and $IrO_2$ are 22, 12, and 50 mV, respectively (**Figure 4b**). In other words, the catalytic activity of $IrB_{1.15}$ in HER surpasses those of commercial Pt/C and $IrO_2$, indicating its superior performance in HER compared to the widely used catalysts. Additionally, the intrinsic catalytic activity of $IrB_{1.15}$ is further demonstrated when normalizing the HER activity by the mass of Ir (**Figure S14**). The Tafel slope of Pt/C (27 mV $dec^{-1}$) is consistent with the reported value,[40] indicating agreement with previous findings (**Figure 4c**). Moreover, $IrB_{1.15}$ shows a slightly lower Tafel slope (25 mV $dec^{-1}$) compared to commercial $IrO_2$ (37.8 mV $dec^{-1}$). Notably, $IrB_{1.15}$ exhibits a Faradaic efficiency (FE) exceeding 98% during the HER (**Figures S15** and **S16**), implying that the observed current can primarily attributed to the electrocatalysis process of HER. To the best of our knowledge, $IrB_{1.15}$ exhibits superior HER performance compared to most other noble-metal-based HER electrocatalysts in acidic aqueous solutions (**Figure 4d** and **Table S2**).

It is worth noting that we further investigated the HER performance of $IrB_{1.15}$ under 4.0 M NaCl at pH =2. As shown in **Figure S17**, compared to its performance in 0.5 M $H_2SO_4$ solution, $IrB_{1.15}$ demonstrates moderate activity, with an overpotential of 68 mV at a geometric current density of 10 mA $cm^{-2}$ and a low Tafel slope of 59 mV $dec^{-1}$ in 4.0 M NaCl at pH 2 (**Figures S17a** and **b**). Furthermore, negligible degradation was observed in the LSV curves of $IrB_{1.15}$ after 1000 CV potential cycles (**Figure S17c**). The chronopotentiometric test presented in **Figure S17d** further demonstrates the excellent HER stability of the $IrB_{1.15}$ catalyst, as it maintains consistent performance over 40 h under 4.0 M NaCl at pH 2 with a current density of nearly 10 mA $cm^{-2}$. Furthermore, an electrolyzer was constructed in a two-electrode configuration, using $IrB_{1.15}$ as both the anodic catalyst for CER and the cathodic catalyst for HER in 4.0 M NaCl at pH =2 and room temperature. As depicted in **Figure S18**, the two-electrode potential of the $IrB_{1.15}$ system achieves 10 mA $cm^{-2}$ at a cell voltage of only 1.51 V, demonstrating outstadanding durability.

Subsequently, the durability of $IrB_{1.15}$ was evaluated by CV at an accelerated scan rate of 100 mV $s^{-1}$. The LSV measurements were performed periodically after 1000 CV cycles, as depicted in **Figure 4e**. It can be observed that the polarization curve of $IrB_{1.15}$ shows almost no degradation following 1000 CV cycles. In addition, the results of long-term electrolysis demonstrate the steady stability of $IrB_{1.15}$, remanning its high performance for at least 110 h (**Figure 4f**).Overall, these results obviously verify that $IrB_{1.15}$ is an outstanding and durable catalyst for HER.

To obtain a comprehensive comprehension of the enhanced catalytic performance of intermetallic $IrB_{1.15}$ for both CER and HER, we constructed relevant structural models encompassing $IrB_{1.15}$ and $IrO_2$ (**Figures 5a-c** and **S19**), followed by conducting DFT calculations. As illustrated in **Figure S20**, the Bader charge analysis suggests an obvious electron rearrangement, suggesting an active electronic interaction between Ir and B elements. According to the previous report, the CER mechanism proceeded by the Volmer ($*/O* + 2Cl^- \rightarrow Cl*/ClO* + Cl^- + e^-$) and subsequent Heyrovsky ($Cl*/ClO* + Cl^- + e^- \rightarrow */O* + Cl_2 + 2e^-$) steps, wherein direct absorption of $Cl^-$ occurred at the active site.[24,41] In this study, Ir sites of $IrB_{1.15}$ were considered for the adsorption of Cl in the DFT calculations. Specifically, as shown in **Figure 5d**, $IrB_{1.15}$ exhibits a moderate Cl adsorption energy of −0.43 eV, which is significantly closer to 0 eV compared to the adsorption energy of Cl on the $IrO_2$ surface (-2.76 eV), thereby indicating a preference for Cl adsorption.[42] More significantly, the in situ Raman spectrum characterization further demonstrated that the Ir sites within $IrB_{1.15}$ function as the primary adsorption sites for Cl. As depicted in **Figure 5e**, with an increase in the reaction potential, a progressively intensified Raman signal originating from of Ir−Cl bond is observed at 500 $cm^{-1}$.[4] Additionally, in the context of HER, a material can exhibit excellent electrocatalyst properties when its Gibbs free energy of hydrogen adsorption ($\Delta G_{H*}$) approaches zero eV.[41] Computational studies indicate that the absolute value of $\Delta G_{H*}$ for $IrB_{1.15}$ is 0.93 eV, which is smaller than that observed for commercial $IrO_2$ (1.17 eV) (**Figure 5f**). In other words, DFT simulations demonstrate that $IrB_{1.15}$ exhibits enhanced catalytic activity for the HER, in accordance with the experimental observations. Similarly, in situ Raman spectra were acquired to analyze intermediates of $IrB_{1.15}$ during the HER process, thereby elucidating the catalytic active sites. The Raman peaks at approximately 432, 511, 882, 981, and 1052 $cm^{-1}$ observed in **Figure 5g**, corresponding to the $H_2SO_4$ electrolytes, exhibit a gradual decrease as the reduction potential increases. The observed phenomena may be attributed to the weakening of $IrH_{ads}$ species with strong binding energy, resulting from the introduction of B atoms to Ir lattices. Consequently, an appropriate Gibbs free energy of hydrogen adsorption on the catalyst surface of $IrB_{1.15}$ is achieved.[17,43] It is worth noting that the Raman peaks at ~750 $cm^{-1}$ in **Figures 5e** and **g** can be attributed to solvent of water.[44,45] Furthermore, the Fermi level crosses the conduction band of $IrO_2$ as demonstrated by the projected density of states (PDOS) (**Figure S21**). The PDOS between commercial $IrO_2$ and $IrB_{1.15}$ indicates enhanced electron mobility in the latter, which is highly significant for electrocatalytic CER or HER activity. As shown in **Figures S21a** and **21b**, unlike the semiconducting behavior observed in $IrO_2$, $IrB_{1.15}$ displays no band gap. Consequently, there is an evident electron transfer from B to Ir within the charge density of $IrB_{1.15}$, resulting in substantial enrichment of electrons. These investigations provide strong evidence that the coupling of B elements significantly influences the electronic structures of Ir in intermetallic compounds of $IrB_{1.15}$, thereby enhancing electron mobility and electrocatalytic activity. In a word, the combined findings unequivocally validate the significant role of light Binduced interstitial effects in enhancing the catalytic performance of intermetallic $IrB_{1.15}$ catalysts for both CER and HER. Additionally, this joule heating techqiues is generally applied for the ultrafast synthesis of many other borides (e.g.,RhB, $Pd_2B$) (**Figure S22**).

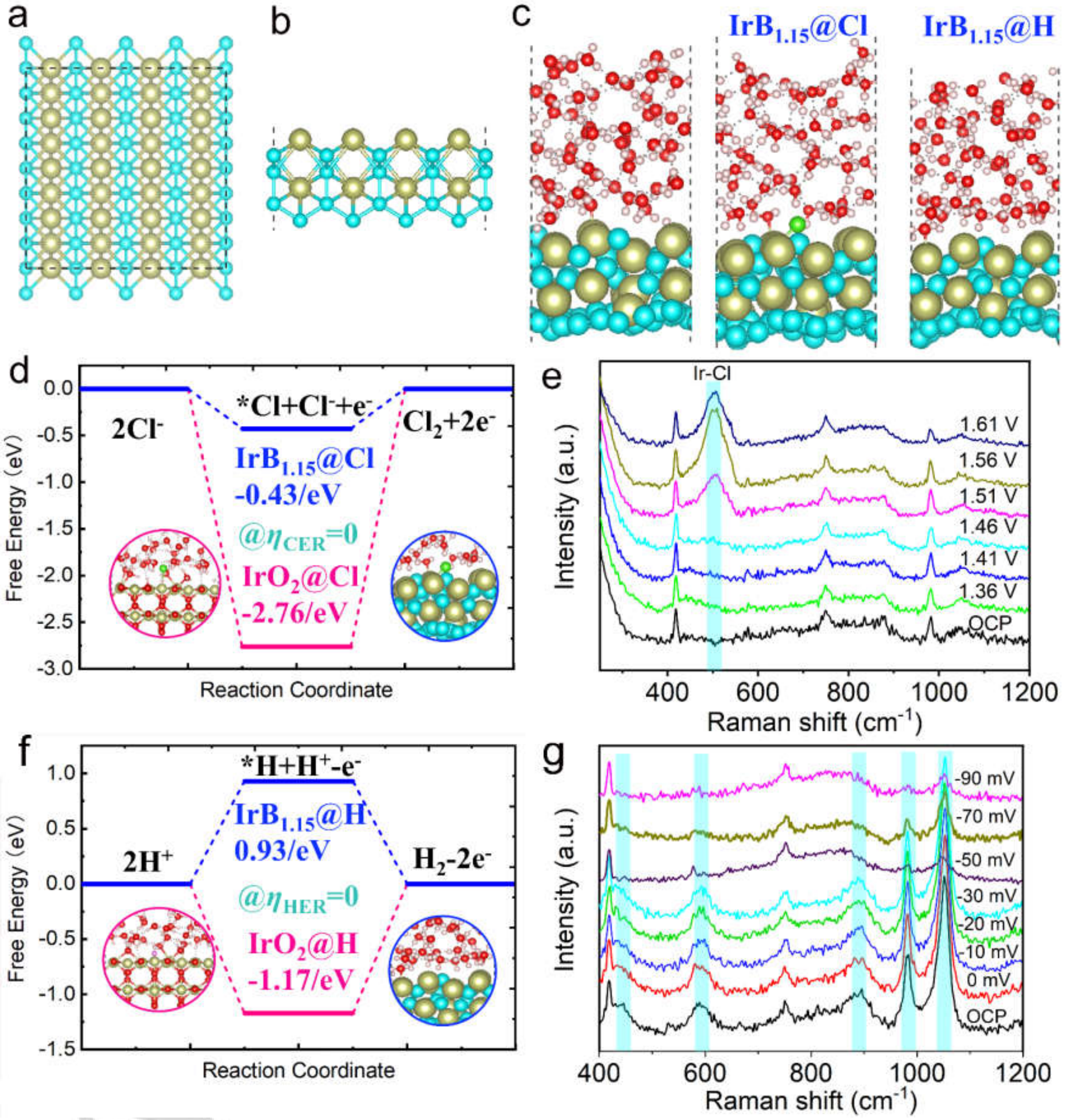

**Figure 5.** (a) side-, and (b) top-down view of the $IrB_{1.15}(110)$ surface. (c) DFT calculation models of the structures of bare $IrB_{1.15}$ surface, $IrB_{1.15}$@Cl, $IrB_{1.15}$@H. (d, f) Free energy diagrams of the (d) CER and (f) HER process over $IrB_{1.15}$ and $IrO_2$, respectively. (e and g) In situ Raman spectrum of $IrB_{1.15}$ collected at (e) CER and (g) HER conditions.

## Conclusion

In summary, the intermetallic compounds of $IrB_{1.15}$ have been successfully synthesized by Joule heating. The obtained $IrB_{1.15}$ material exhibits outstanding catalytic activity and robust stability toward both CER and HER. It only needs overpotentials of 75 and 12 mV to produce an operationally relevant current density of 10 mA $cm^{-2}$ 4.0 M NaCl and 0.5 M $H_2SO_4$ solutions, respectively. These exceptional catalytic properties not only rival those of state-of-the-art commercial catalysts, such as $IrO_2$ and Pt/C but also exhibit superior long-term durability compared to these commercially available electrocatalysts. Mechanism studies showed that the presence of Ir in $IrB_{1.15}$ serves as the active center for CER. Moreover, the introduction of B atoms to

Ir lattices can attenuate the formation of absorbed hydrogen species on the Ir surface, thereby enabling excellent performance in HER for $IrB_{1.15}$ material. Furthermore, theoretical studies have confirmed that $IrB_{1.15}$ demonstrates more favorable adsorption energies towards Cl and H, respectively, in comparison to $IrO_2$ and Pt/C. These findings serve as the primary factors contributing to the enhanced catalytic activity of $IrB_{1.15}$ in both CER and HER. Undoubtedly, the catalytic activity exhibited by the intermetallic compounds of $IrB_{1.15}$ paves a novel pathway for the design of metal boride materials, which were synthesized by Joule heating and exceptional performance toward CER, HER, and other related electrocatalytic applications.

## Acknowledgements

This work was supported by the National Natural Science Foundation of China (Grant No. 22402030), Institut National de la Recherche Scientifique (INRS), and Fonds de Recherche du Québec-Nature et Technologies (FRQNT).

## Conflicts of interest

The authors declare no competing financial interest.

**Keywords:** intermetallic compounds • Joule heating • chlorine evolution reaction • hydrogen evolution reaction• saline water

## References

[1] R. K. Karlsson, A. Cornell, *Chem. Rev.* **2016**, *116*, 2982–3028.
[2] Z. Jakub, J. Hulva, M. Meier, R. Bliem, F. Kraushofer, M. Setvin, M. Schmid, U. Diebold, C. Franchini, G. S. Parkinson, *Angew. Chem. Int. Ed.* **2019**, *58*, 13961−13968.
[3] Y. Yao, L. Zhao, J. Dai, J. Wang, C. Fang, G. Zhan, Q. Zheng, W. Hou, L. Zhang, *Angew. Chem. Int. Ed.* **2022**, *61*, e202208215.
[4] J. Wang, L. Zhao, Y. Zou, J. Dai, Q. Zheng, X. Zou, L. Hu, W. Hou, R. Wang, K. Wang, Y. Shi, G. Zhan, Y. Yao, L. Zhang, *J. Am. Chem. Soc.* **2024**, *146*, 11152−11163.
[5] J. Yang, W. Li, H. Tang, Y. Pan, D. Wang, Y. Li, *Nature* **2023**, *617*, 519–523.
[6] J. Crook, A. Mousavi, *Environ. Forensics* **2016**, *17*, 211–217.
[7] S. Anantharaj, S. Noda, V. R. Jothi, S. Yi, M. Driess, P. W. Menezes, *Angew. Chem. Int. Ed.* **2021**, *60*, 18981-19006.
[8] I. T. McCrum, M. T. M. Koper, *Nat. Energy* **2020**, *5*, 891–899.
[9] T. Wang, L. Tao, X. Zhu, C. Chen, W. Chen, S. Du, Y. Zhou, B. Zhou, D. Wang, C. Xie, P. Long, W. Li, Y. Wang, R. Chen, Y. Zou, X. Fu, Y. Li, X. Duan, S. Wang, *Nat. Catal.* **2022**, *5*, 66–73.
[10] L. Shen, B. Lu, Y. Li, J. Liu, Z. Huang, H. Peng, J. Ye, X. Qu, J. Zhang, G. Li, W. Cai, Y. Jiang, S. Sun, *Angew. Chem. Int. Ed.* **2020**, *59*, 22397-22402.
[11] K. S. Exner, J. Anton, T. Jacob, H. Over, *Angew. Chem. Int. Ed.* **2014**, *126*, 11212-11215.
[12] T. Lim, G. Y. Jung, J. H. Kim, S. O. Park, J. Park, Y. T. Kim, S. J. Kang, H. Y. Jeong, S. K. Kwak, S. H. Joo, *Nat. Commun.* **2020**, *11,* 412.
[13] M. Jiang, H. Wang, Y. Li, H. Zhang, G. Zhang, Z. Lu, X. Sun, L. Jiang, *Small* **2017**, *13*, 1602240–1602247.
[14] S. Choi, W. I. Choi, J. S. Lee. C. H. Lee, M. Balamurugan, A. D. Schwarz, Z. S. Choi, H. Randriamahazaka, K. T. Nam, *Adv. Mater.* **2023**, *35*, 23004291.
[15] T. Loučka, *J. Appl. Electrochem.* **1990**, *20*, 522–523.
[16] Y. Wen, P. Chen, L. Wang, S. Li, Z. Wang, J. Abed, X. Mao, Y. Min, C. T. Dinh, P. D. Luna, R. Huang, L. Zhang, L. Wang, L. Wang, R. J. Nielsen, H. Li, T. Zhuang, C. Ke, O. Voznyy, Y. Hu, Y. Li, W. A. Goddard III, B. Zhang, H. Peng, E. H. Sargent, *J. Am. Chem. Soc.* **2021**, *143*, 6482–6490.
[17] Z. Pu, J. Zhao, I. S. Amiinu, W. Li, M. Wang, D. He, S. Mu, *Energy Environ. Sci.* **2019**, *12*, 952-957.
[18] K. Kawashima, R. A. Márquez, L. A. Smith, R. R. Vaidyula, O. A. Carrasco-Jaim, Z. Wang, Y. J. Son, C. L. Cao, C. B. Mullins, *Chem. Rev.* **2023**, *123*, 12795–13208.
[19] T. Zheng, C. Shang, Z. He, X. Wang, C. Cao, H. Li, R. Si, B. Pan, S. Zhou, J. Zeng, *Angew. Chem. Int. Ed.* **2019**, *131*, 14906-14911.
[20] D. Chen, Z. Pu, P. Wang, R. Lu, W. Zeng, D. Wu, Y. Yao, J. Zhu, J. Yu, P. Ji, S. Mu, *ACS Catal.* **2022**, *12*, 2623–263.
[21] E. Rahman, J. Shin, S. Hong, S. Im, J. Kim, C. Chung, S. W. Hong, M. R. Hoffmann, K. Cho, *ACS Catal.* **2024**, *14*, 8427–8436.
[22] Z. Yu, G. Xia, V. M. Diaconescu, L. Simonelli, A. P. LaGrowbf, Z. Taib, X. Xianga, D. Xiong, L. Liu, *Chem. Sci.* DOI: 10.1039/D4SC01220H.
[23] J. S. Ko, J. K. Johnson, P. I. Johnson, Z. Xia, *ChemCatChem* **2020**, *12*, 4526-4532.
[24] M. Xiao, Q. Wu, R. Ku, L. Zhou, C. Long, J. Liang, A. Mavrič, L. Li, J. Zhu, M. Valant, J. Li, Z. Zeng, C. Cui, *Nat. Commun.* **2023**, *14*, 5356.
[25] L. T. Alameda, K. J. Baumler, R. R. Katzbaer, R. E. Schaak, *Acc. Chem. Res.* **2023**, *56*, 3515–3524.
[26] C. Sekhar Rout, P. V. Shinde, A. Patra, S. Mun Jeong, *Adv. Sci.* **2024**, *11*, 2308178.
[27] Y. Wang, M. Zhang, Z. Kang, L. Shi, Y. Shen, B. Tian, Y. Zou, H. Chen, X. Zou, *Nat. Commun.* **2023**, *14*, 5119.
[28] E. Lee, B. P. T. Fokwa, *Acc. Chem. Res*. **2022**, *55*, 1, 56–64.
[29] B. Aronsson, E. Stenberg, J. Åselius, *Nature* **1962**, *195*, 377–378.
[30] Q. Dong, Y. Yao, S. Cheng, K. Alexopoulos, J. Gao, S. Srinivas, Y. Wang, Y. Pei, C. Zheng, A. H. Brozena, H. Zhao, X. Wang, H. E. Toraman, B. Yang, I. G. Kevrekidis, Y. Ju, D. G. Vlachos, D. Liu, L. Hu, *Nature* **2022**, *605,* 470–476.
[31] M. Cui, C. Yang, S. Hwang, B. Li, Q. Dong, M. Wu, H. Xie, X. Wang, G. Wang, L. Hu, *Nano Lett.* **2022**, *22*, 255–262.
[32] M. Cui, C. Yang, S. Hwang, M. Yang, S. Overa, Q. Dong, Y. Yao, A. H. Brozena, D. A. Cullen, M. Chi, T. F. Blum, D. Morris, Z. Finfrock, X. Wang, P. Zhang, V. G. Goncharov, X. Guo, J. Luo, Y. Mo, F. Jiao, L. Hu, *Sci. Adv.* **2022**, *8*, eabm4322.
[33] B. Deng, Z. Wang, W. Chen, J. T. Li, D. X. Luong, R. A. Carter, G. Gao, B. I. Yakobson, Y. Zhao, J. M. Tour, *Nat. Commun.* **2022**, *13*, 262.
[34] K. M. Wyss, D. X. Luong, J. M. Tour, *Adv. Mater.* **2022**, *34*, 2106970.
[35] C. H. Choi, J. Shin, L. Eddy, V. Granja, K. M. Wyss, B. Damasceno, H. Guo, G. Gao, Y. Zhao, C. F. Higgs III, Y. Han, J. M. Tour, *Nat. Chem.* **2024**, DOI.org/10.1038/s41557-024-01598-7.
[36] D. Chen, R. Yu, H. Zhao, J. Jiao, X. Mu, J. Yu, S. Mu, *Angew. Chem. Int. Ed.* DOI:10.1002/anie.202407577.
[37] D. Chen, T. Liu, P. Wang, J. Zhao, C. Zhang, R. Cheng, W. Li, P. Ji, Z. Pu, S. Mu, *ACS Energy Lett.* **2020**, *5*, 2909–2915.

[38] S. J. Freakley, J. Ruiz-Esquius, D. J. Morgan, *Surf. Interface Anal.* **2017**, *49*, 794-799.

[39] C. Andronescu, S. Barwe, E. Ventosa, J. Masa, E. Vasile, B. Konkena, S. Möller, W. Schuhmann, *Angew. Chem. Int. Ed.* **2017**, *56*, 11258-11262.

[40] H. Wu, C. Feng, L. Zhang, J. Zhang, D. P. Wilkinson, *Electrochem. Energy Rev*. **2021**, *4*, 473–507.

[41] J. Yang, W. Li, K. Xu, S. Tan, D. Wang, Y. Li, *Angew Chem. Int. Ed*. **2022**, *134*, e202200366.

[42] K. S. Exner, *J. Phys. Chem. C* **2019**, *123*, 16921−16928.

[43] H. Bai, D. Chen, Q. Ma, R. Qin, H. Xu, Y. Zhao, J. Chen, S. Mu, *Electrochem. Energy Rev*. **2022**, *5*, 24.

[44] K. H. Cho, S. Park, H. Seo, S. Choi, M. Y. Lee, C. Ko, K. T. Nam, *Angew Chem. Int. Ed*. **2021**, *60*, 4673-4681.

[45] D. Chen, R. Yu, K. Yu, R. Lu, H. Zhao, J. Jiao, Y. Yao, J. Zhu, J. Wu, S. Mu, *Nat. Commun*. **2024**, *15*, 3928.

## Entry for the Table of Contents

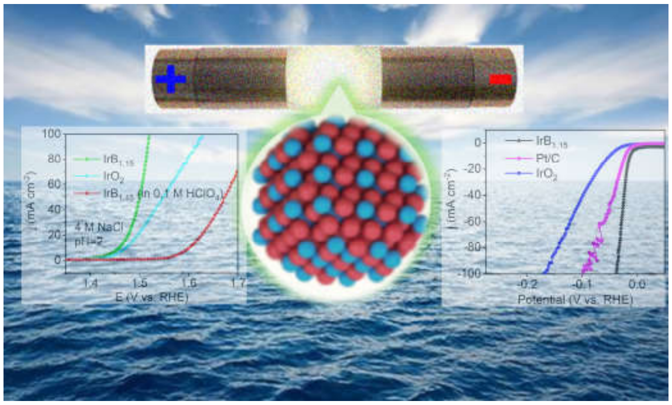

Intermetallic compounds of $IrB_{1.15}$ have been successfully synthesized by ultrafast Joule heating at 900 ℃ for a duration of 12 seconds, showcasing their robust electrocatalytic performance in acidic saline water media for both chlorine and hydrogen evolution reactions.